Chalmers Publication Library

Copyright Notice

An Optimal Beamforming Strategy for Wide-Field Surveys With Phased-Array-Fed Reflector Antennas

M. V. Ivashina, O. Iupikov, R. Maaskant, W. A. van Cappellen, and T. Oosterloo

Abstract— An optimal beamforming strategy is proposed for performing large-field surveys with dual-polarized phased-array-fed reflector antennas. This strategy uses signal-processing algorithms that maximize the beam sensitivity and the continuity of a Field-Of-View (FOV) which is formed by multiple closely overlapping beams. A mathematical framework and a newly developed numerical approach are described to analyze and optimize a Phased Array Feed (PAF) system. The modelling approach has been applied to an experimental PAF system (APERTIF prototype) which is installed on the Westerbork Synthesis Radio Telescope. The resulting beam shapes, sensitivity, and polarization diversity characteristics (such as the beam orthogonality and the intrinsic cross-polarization ratio) are examined over a large FOV and frequency bandwidth. We consider weighting schemes to achieve a conjugate-field matched situation (max. received power), maximum SNR, and a reduced SNR scenario but with constraints on the beam shape. The latter improves the rotational symmetry of the beam and reduces the sensitivity ripple, at a modest maximum sensitivity penalty. The obtained numerical results demonstrate a very good agreement with the measurements performed at the telescope.

Index Terms— reflector antenna feeds, antenna arrays, array signal processing, system modeling techniques, polarimetry, radio astronomy, phased array feeds, focal plane arrays.

I. INTRODUCTION

PRESENT day aperture synthesis radio telescopes have limited survey capabilities because they can observe only a small region of the sky for each beam pointing. The survey speed of reflector telescopes can be greatly increased by installing a phased array feed (PAF) in the focal plane to perform instantaneous multibeaming. The increased survey speed enables new astronomical science, in particular wide-field surveys on short timescales will be within reach [1], [2], [3].

The effectiveness of performing wide-field surveys is characterized by the telescope's survey speed, i.e., the speed at which a certain volume of space can be observed at a given sensitivity. The survey speed is proportional to the size of the instantaneous FOV and the frequency bandwidth, weighted by the sensitivity squared [4].

M. V. Ivashina, R. Maaskant W. A. van Cappellen, and T. Oosterloo are with the Netherlands Institute for Radio Astronomy (ASTRON), P.O. Box 2, 7990 AA Dwingeloo, The Netherlands. M. V. Ivashina is now with the Department of Space and Earth Science and R. Maaskant is with the Department of Signals and Systems of the Chalmers University of Technology, Sweden (ivashina@chalmers.se; marianna.ivashina@gmail.com; maaskant@chalmers.se, cappellen@astron.nl, oosterloo@astron.nl)

O. Iupikov is with the Sevastopol National Technical University, Radio Engineering Dept., Streletskaya balka, Studgorodok, Sevastopol, 99053, Ukraine (liche@gmail.com).

The FOV of conventional telescopes with single-beam feeds is limited to one half-power beamwidth, where the sensitivity takes the maximum value along the beam axis and gradually decreases from its center. To image a larger region of the sky, astronomers use the "mosaicing" technique [5]. With this technique a telescope performs many observations by mechanically steering (scanning) the dish such that the main-lobes of the beams generated in subsequent observations closely overlap and form an almost continuous envelope when superimposed. The large-field image is therefore formed by composing a mosaic of smaller sized overlapping images taken during these observations. According to Nyquist's field-sampling theorem, a uniform sensitivity of the combined image is achieved when the beam separation is equal to or smaller than one half of the half-power beamwidth. A larger spacing between the observations results in a sensitivity ripple over the FOV. The maximum allowable ripple will depend on the particular science case. In this paper it is assumed that the sensitivity ripple is required to be less than $\sim 20\%$.

PAFs can provide many closely overlapping beams in one snapshot, thereby greatly improving the size of the FOV. However, to meet the required field-sampling limit with a cost-effective number of PAF beams, their shapes should be optimized and the maximum achievable sensitivity should be traded against the maximum tolerable sensitivity ripple over the FOV.

In addition to a continuous FOV and high sensitivity, a high polarization discrimination is required for large-field surveys. For this purpose, the incident field is sampled by two orthogonally polarized receptors or beams. In radio astronomy the polarization purity of the resulting images is established after extensive off-line calibration of the data. In this respect, two antenna design aspects are of particular importance: the stability (i.e. variation over time) of the co- and cross-polarized beams; and the orthogonality of the two beams in the direction of incidence. This requires that the beams are formed simultaneously and span a 2D basis along which the incident field is decomposed. Future PAF-equipped telescopes are potentially accurate polarimeters thanks to the flexibility that digital beamforming offers. However, although the orthogonality of the beam pair in the direction of observation may be improved electronically, it is important that the intrinsic polarization characteristics of the beams are sufficiently good to minimize such corrections as they may compromise the receiving sensitivity.

In this paper we describe and model the performance of the APERTIF ("APERture Tile In Focus") PAF system, which is currently being developed and will be installed on the

Westerbork Synthesis Radio Telescope (WSRT). The aim of APERTIF is to increase the survey speed of the WSRT by a factor of 20 to enable deep all-northern-sky surveys in the 1.0 to 1.7 GHz frequency band. Preliminary modeling and experimental results obtained for the first APERTIF prototype have been reported in [6], [7]. This paper presents results of the second PAF prototype, which is comprised of 144 tapered slot antenna (TSA) elements. First, we propose a beamforming strategy for maximizing the beam sensitivity and its continuity over the FOV. This algorithm has been implemented in a newly developed numerical toolbox for the CAESAR software[1] to interface with GRASP9 (TICRA's commercially available software tool) and perform a PAF system analysis and optimization. Afterwards, the numerical results are discussed and verified against the measurements of an APERTIF prototype in a WSRT antenna. Finally, the polarimetric properties of the prototype are modeled.

In this paper, the term *primary pattern* refers to the far-field radiation pattern of the feed illuminating the reflector (assuming no feed-reflector interaction). The *secondary pattern* is the resulting far-field radiation pattern on the sky after the primary radiated field is reflected from the dish.

II. OPTIMAL BEAMFORMING STRATEGY

A. Mathematical framework

Antenna systems are often optimized by describing their performance figures-of-merit as ratios of quadratic forms. This concept originates from the 50's–60's [9], [10] and has been widely used in modern radar, wireless systems [11], and recently for radio astronomy [12]. To outline the optimization procedure for the PAF beamformers considered in this paper, we utilize the generalized system representation as shown in Fig. 1 for the N actively beamformed antennas.

The system is subdivided into two blocks: (i) the frontend including the reflector, array feed, Low Noise Amplifiers (LNAs); and (ii) the beamformer with complex conjugated weights $\{w_n^*\}_{n=1}^N$ and an ideal (noiseless/reflectionless) power combiner realized in software. Here, $\mathbf{w}^H = [w_1^*, \ldots, w_N^*]$ is the beamformer weight vector, H is the Hermitian transpose, and the asterisk denotes the complex conjugate. Furthermore, $\mathbf{a} = [a_1, \ldots, a_N]^T$ is the vector holding the transmission-line voltage-wave amplitudes at the beamformer input (the N LNAs outputs). Thence, the fictitious beamformer output voltage v (across Z_0) can be written as $v = \mathbf{w}^H \mathbf{a}$, and the receiver output power as $|v|^2 = vv^* = (\mathbf{w}^H\mathbf{a})(\mathbf{w}^H\mathbf{a})^* = (\mathbf{w}^H\mathbf{a})(\mathbf{a}^T\mathbf{w}^*)^* = \mathbf{w}^H\mathbf{a}\mathbf{a}^H\mathbf{w}$, where the proportionality constant has been dropped as this is customary in array signal processing and because we will consider only ratio of powers.

Although each subsystem can be rather complex and contain multiple internal signal/noise sources, it is characterized externally (at its accessible ports) by a scattering matrix in conjunction with a noise- and signal-wave correlation matrix. In this

manner, the system analysis and weight optimization becomes a purely linear microwave-circuit problem. The sensitivity
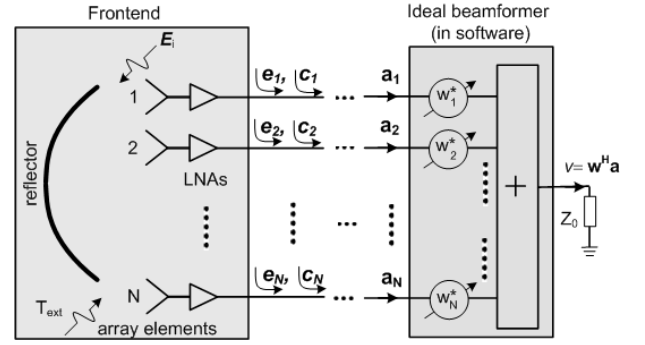

Fig. 1. Generalized representation of the PAF system.

metric $A_{\text{eff}}/T_{\text{sys}}$, which is the effective area of the antenna system divided by the system equivalent noise temperature, can be expressed in terms of the Signal-to-Noise Ratio (SNR) and the normalized flux density S_{source} of the source (in Jansky, $1\,[\text{Jy}] = 10^{-26}\,[\text{Wm}^{-2}\text{Hz}^{-1}]$) as

$$\frac{A_{\text{eff}}}{T_{\text{sys}}} = \frac{2k_{\text{B}}}{S_{\text{source}}}\text{SNR}, \quad \text{where} \quad \text{SNR} = \frac{\mathbf{w}^H\mathbf{P}\mathbf{w}}{\mathbf{w}^H\mathbf{C}\mathbf{w}}, \quad (1)$$

and where k_B is Boltzmann's constant. The SNR function is defined as a ratio of quadratic forms where $\mathbf{C}$ is a Hermitian spectral noise-wave correlation matrix holding the correlation coefficients between the array receiver channels, i.e., $C_{mk} = \mathsf{E}\{c_m c_k^*\} = \overline{c_m c_k^*}$ (for $k, m = 1 \ldots N$). Here, c_m is the complex-valued voltage amplitude of the noise wave emanating from channel m (see [13] and references therein), which includes the external and internal noise contributions inside the frontend block in Fig. 1. We consider only a narrow frequency band, and assume that the statistical noise sources are (wide-sense) stationary random processes which exhibit ergodicity, so that the statistical expectation can be replaced by a time average (as also exploited in hardware correlators). $\mathbf{C}$ is nonzero if noise sources are present in the external environment and inside the system, due to e.g. the ground, LNAs, and sky (see Fig. 1). For a single point source on the sky, the signal-wave correlation matrix $\mathbf{P} = \mathbf{e}\mathbf{e}^H$ is a one-rank positive semidefinite matrix. The vector $\mathbf{e} = [e_1, e_2, .., e_N]^T$ holds the signal-wave amplitudes at the receiver outputs and arises due to an externally applied plane electromagnetic wave E_{i}.

1) Maximum Sensitivity in the Main Beam Center: Maximizing Eq. (1) amounts to solving the largest root of the determinantal equation: $\det(\mathbf{P} - \text{SNR}\,\mathbf{C}) = 0$ (*cf.* [9]). Next, the optimum beamfomer weight vector $\mathbf{w}_{\text{MaxSNR}}$ is found through solving the corresponding generalized eigenvalue equation $\mathbf{P}\mathbf{w}_{\text{MaxSNR}} = \text{SNR}\,\mathbf{C}\mathbf{w}_{\text{MaxSNR}}$ for the largest eigenvalue (SNR) as determined in the previous step. The well-known closed-form solution for the point source case, where $\mathbf{P}$ is of rank 1, is given by [9]

$$\mathbf{w}_{\text{MaxSNR}} = \mathbf{C}^{-1}\mathbf{e}, \quad \text{with} \quad \text{SNR} = \mathbf{e}^H\mathbf{w}_{\text{MaxSNR}} \quad (2)$$

where the eigenvector $\mathbf{e}$ corresponds to the largest eigenvalue of $\mathbf{P}$. When $\mathbf{C}$ equals the identity matrix $\mathbf{I}$ (thus equal and uncorrelated output noise powers), the receiver output noise power $\mathbf{w}^H \mathbf{C} \mathbf{w} = \mathbf{w}^H \mathbf{w}$ becomes independent of $\mathbf{w}$ in case its 2-norm $\mathbf{w}^H \mathbf{w}$ is a constant value, typically chosen to be unity. With reference to (2), the weight vector that maximizes the received power, and thus realizes a maximum directive gain (and effective area) in the direction of observation, is therefore

$$\mathbf{w}_{\mathrm{CFM}} = \mathbf{e}. \tag{3}$$

These weights optimally satisfy the Conjugate Field Matching (CFM) condition [14], [15].

2) Maximum Sensitivity and Constraints on the Beam Shape: The optimal beamformer weights in (2) maximize the sensitivity in the beam centers. However, no constraint is posed on the sensitivity variation within the beamwidth, so that a smooth transition between the adjacent beams cannot be guaranteed. To improve the uniformity of the FOV, constraints are imposed at the beam cross-over points to increase the sensitivity in these directions, while accepting a minor sensitivity loss in the beam center. For this purpose, the linear constrained minimum variance (LCMV) beamforming scheme can be used [11, pp. 513–517]. In this case, the beamformer weight vector with directional constraints is computed as [11, p. 527]

$$\mathbf{w}_{\mathrm{MaxSNR\&Constr}}^H = \mathbf{g}^H \left[\mathbf{G}^H \mathbf{C}^{-1} \mathbf{G} \right]^{-1} \mathbf{G}^H \mathbf{C}^{-1} \tag{4}$$

where $\mathbf{G}$ is the directional constraint matrix of size $N \times N_{\mathrm{dir}}$, whose columns are the signal vectors for the N_{dir} directions $\{\Omega_i\}_{i=1}^{N_{\mathrm{dir}}}$, that is,

$$\mathbf{G} = \left[\mathbf{e}(\Omega_1) \ \vdots \ \mathbf{e}(\Omega_2) \ \vdots \ \cdots \ \vdots \ \mathbf{e}(\Omega_{N_{\mathrm{dir}}}) \right]. \tag{5}$$

The entries of vector

$$\mathbf{g} = [g_1, \ g_2, \ \cdots, \ g_{N_{\mathrm{dir}}}]^T \tag{6}$$

are the values of the constraints, where g_1 corresponds to the maximum sensitivity direction (at the center of the beam) and is usually set to unity, while the remaining directional constraints are relative to this value and set by the requirements if the maximum allowable sensitivity ripple over the FOV.

B. Measurement procedure

The optimal weight vectors described above can be determined once the signal vector $\mathbf{e}$ and the noise-wave correlation matrix $\mathbf{C}$ are known. These quantities are indirectly measurable through a two-stage measurement procedure that has been proposed by K. Warnick *et al.* [16]. We will generalize their procedure to also determine the constraint matrix $\mathbf{G}$. The procedure is as follows:

- *Step 1*: The telescope is pointed at a bright point source in the direction Ω_1 and the full correlation matrix $\mathbf{C}_{\mathrm{on}} = \mathbf{P} + \mathbf{C}$ is measured. Here, $\mathbf{C}_{\mathrm{on}}$ incorporates the combined response of all noise sources (internal and external to the system) as well as the signal of interest. $\mathbf{P}$ is the signal-wave correlation matrix.

- *Step 2:* The matrix $\mathbf{C}$ can be measured separately by rotating the dish away from the strong point source and to observe an empty part of the sky. Preferably this location is close to the point source used in step 1 to minimize variation of the spillover noise with elevation.
- *Step 3:* Assuming a time-invariant system, $\mathbf{P} = \mathbf{C}_{\mathrm{on}} - \mathbf{C}$. The signal vector $\mathbf{e}$ is determined from $\mathbf{P}$ by maximizing the beamformer output power $\mathbf{w}^H \mathbf{P} \mathbf{w}$. On account of Eq. (3), this is achieved if $\mathbf{w} = \mathbf{e}$. In other words, $\mathbf{e}$ is found as the dominant eigenvector of $\mathbf{P}$.
- *Step 4:* Now that $\mathbf{C}$ and $\mathbf{e}$ are known, the beamformer weights to achieve maximum sensitivity can be computed from Eq. (2). Alternatively, to determine the optimal weight vector (4), one needs to compute the columns of matrix $\mathbf{G}$ by repeating *Step 3* for the remaining $N_{\mathrm{dir}} - 1$ directions of constraints.

Steps 3 and *4* in the above procedure need to be repeated for each beam within the FOV. However, because beams partially overlap, the total number of measurements in the directional constraint case can be significantly reduced by realizing that some directions are common to multiple beams.

C. Polarization Discrimination Figure Of Merit

One of our objectives is to analyze the polarization discrimination capabilities of the instrument. To this end, the beamformer in Fig. 1 is extended to have two outputs. We consider a distinct pair of weight vectors, *viz.*, $\mathbf{w}^p$, with $p \in \{\mathrm{CO}, \mathrm{XP}\}$. The CO and XP superscripts refer to the externally applied plane electromagnetic wave $\boldsymbol{E}_i$, whose polarization is either $\widehat{\boldsymbol{E}}_i^{\mathrm{CO}}$ or $\widehat{\boldsymbol{E}}_i^{\mathrm{XP}}$ and have unit intensity. These are the pair of unit basis vectors of the orthogonal Ludwig-3 reference frame [17]. The weight vector $\mathbf{w}^{\mathrm{CO}}$ is determined, so as to optimally receive $\widehat{\boldsymbol{E}}_i^{\mathrm{CO}}$ according to a certain criterion (see Sec. II). Likewise, $\mathbf{w}^{\mathrm{XP}}$ optimally receives $\widehat{\boldsymbol{E}}_i^{\mathrm{XP}}$. Afterwards, we let $\widehat{\boldsymbol{E}}_i^{\mathrm{CO}}$ be incident and use the weight vector $\mathbf{w}^{\mathrm{XP}}$ to analyze the polarization leakage at the XP beamformer output. We perform the same procedure at the CO beamformer output for the weight vector $\mathbf{w}^{\mathrm{CO}}$ for $\widehat{\boldsymbol{E}}_i^{\mathrm{XP}}$. In summary, we consider the beamformer output voltage vectors $\mathbf{v}^{\mathrm{CO}}$ and $\mathbf{v}^{\mathrm{XP}}$, which are the system responses to co- and cross-polarized incident fields $\widehat{\boldsymbol{E}}_i^{\mathrm{CO}}$ and $\widehat{\boldsymbol{E}}_i^{\mathrm{XP}}$, respectively. The elements of these output voltages vectors are computed as

$$\mathbf{v}^p = \begin{bmatrix} v_1^p \\ v_2^p \end{bmatrix} = \begin{bmatrix} \left(\mathbf{w}^{\mathrm{CO}} \right)^H \mathbf{e}^p \\ \left(\mathbf{w}^{\mathrm{XP}} \right)^H \mathbf{e}^p \end{bmatrix} \quad \text{for } p \in \{\mathrm{CO}, \mathrm{XP}\}. \tag{7}$$

Ideally, one expects $\mathbf{v}^{\mathrm{CO}}$ to be directly proportional to $\widehat{\boldsymbol{E}}_i^{\mathrm{CO}}$, and that $\mathbf{v}^{\mathrm{XP}}$ is a measure for $\widehat{\boldsymbol{E}}_i^{\mathrm{XP}}$, but this may not be the case due to an instrumental polarization leakage. Indeed, we know that $\left(\widehat{\boldsymbol{E}}_i^{\mathrm{CO}} \right)^H \widehat{\boldsymbol{E}}_i^{\mathrm{XP}} = 0$, but $\mathbf{v}^{\mathrm{CO}}$ and $\mathbf{v}^{\mathrm{XP}}$ may not be perfectly orthogonal. The degree of orthogonality can be conveniently measured through the normalized cross-correlation term [18]

$$\rho_{\mathrm{cor}} = \frac{\langle \mathbf{v}^{\mathrm{CO}}, \mathbf{v}^{\mathrm{XP}} \rangle}{\sqrt{\langle \mathbf{v}^{\mathrm{CO}}, \mathbf{v}^{\mathrm{CO}} \rangle \langle \mathbf{v}^{\mathrm{XP}}, \mathbf{v}^{\mathrm{XP}} \rangle}} \tag{8}$$

where $\langle \boldsymbol{a}, \boldsymbol{b} \rangle = \boldsymbol{a}^* \cdot \boldsymbol{b} = \boldsymbol{a}^H \boldsymbol{b}$ represents the Hermitian inner product. Note, however, that ρ_{cor} measures the orthogonality of beams and does not account for a magnitude difference (differential beam gain).

To account for magnitude differences, the independence between $\mathbf{v}^{\text{CO}}$ and $\mathbf{v}^{\text{XP}}$ can be measured through the condition number κ of the 2×2 column-augmented matrix[2]

$$\mathbf{J} = [\mathbf{v}^{\text{CO}} \,\vdots\, \mathbf{v}^{\text{XP}}] = \begin{bmatrix} (\mathbf{w}^{\text{CO}})^H \mathbf{e}^{\text{CO}} & (\mathbf{w}^{\text{CO}})^H \mathbf{e}^{\text{XP}} \\ (\mathbf{w}^{\text{XP}})^H \mathbf{e}^{\text{CO}} & (\mathbf{w}^{\text{XP}})^H \mathbf{e}^{\text{XP}} \end{bmatrix} \quad (9)$$

where (7) has been substituted. Since $\kappa(\mathbf{J}) \geq 1$, a more appropriate measure yielding values between unity and infinity is the so-called intrinsic cross-polarization ratio (IXR) as proposed by Carozzi [20], i.e.,

$$\text{IXR}_J = \left(\frac{\kappa(\mathbf{J}) + 1}{\kappa(\mathbf{J}) - 1} \right)^2. \quad (10)$$

The IXR measures the orthogonality between channels and also accounts for differential channel gains. The IXR can be understood as the worst-case cross-polarization ratio of a given polarimeter before calibration, and it is closely related to the total relative error of the fully calibrated polarimeter [20].

III. PAF-SYSTEM SIMULATOR (PAFS) FOR ANALYSIS AND OPTIMIZATION

This section describes a procedure to simulate PAF receiving systems, and to optimize their beamformer weights. For this purpose, CAESAR's combined MoM and circuit solver as presented in [21] has been extended and interfaced with GRASP [33]. Fig. 2 illustrates the general diagram of the implemented algorithm, where the first block lists the required input parameters: (i) the simulated or measured impedance matrix $\mathbf{Z}_{\text{ant}}$ and the embedded element patterns $\{\boldsymbol{f}_n(\Omega)\}_{n=1}^N$ of the considered antenna array. Each of these patterns was obtained by exciting the respective element with a 1 Ampère current source while open-circuiting the others; (ii) the orthogonal set of incident fields $\boldsymbol{E}_{\text{i}} \in \{\widehat{\boldsymbol{E}}_{\text{i}}^{\text{CO}}, \widehat{\boldsymbol{E}}_{\text{i}}^{\text{XP}}\}$; and (iii) the direction-dependent noise temperature distribution $T_{\text{ext}}(\Omega)$ of the external environment (due to external noise sources on the sky and ground).

The five-stage analysis and optimization procedure begins by calculating the noise-wave power correlation matrix $\mathbf{C}_{\text{ant}}$ of the reflector-array antenna system (excluding the receiver) due to external noise sources as follows:

$$\mathbf{C}_{\text{ant}} = \mathbf{L}\mathbf{V}_{\text{ant}}\mathbf{L}^H \quad (11)$$

where the matrix $\mathbf{L} = \sqrt{Z_o}(\mathbf{Z}_{\text{ant}} + Z_o \mathbf{I})^{-1}$ accomplishes the voltage- to noise-wave transformation for the real-valued scalar reference impedance Z_o, and $\mathbf{V}_{\text{ant}}$ is the $N \times N$ antenna noise voltage correlation matrix. Each element of $\mathbf{V}_{\text{ant}}$ is computed through a pattern-overlap integral between the mth and nth array element patterns [21]:

$$V_{mn} = \frac{k_B}{2\pi^2 \eta_0} \int_\Omega T_{\text{ext}}(\Omega) \left[\boldsymbol{f}_m(\Omega) \cdot \boldsymbol{f}_n^*(\Omega) \right] d\Omega \quad (12)$$

[2]The matrix $\mathbf{J}$ is the Jones matrix of the polarimeter [19].
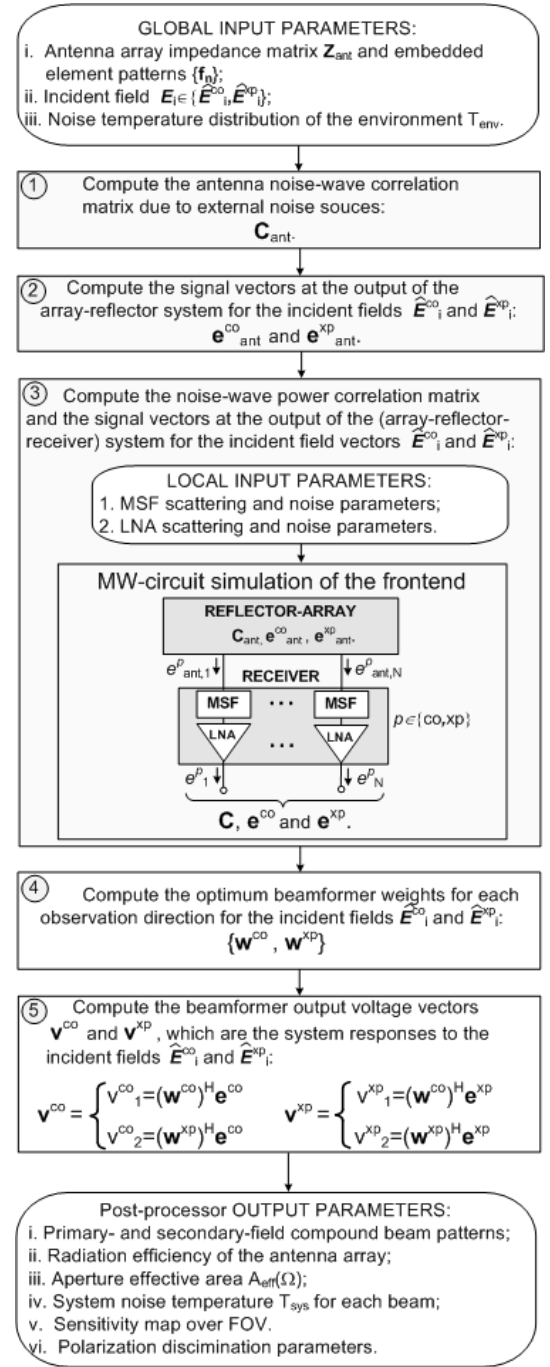

Fig. 2. Block-diagram of the algorithm realized in the CAESAR-GRASP PAF Toolbox for sensitivity analysis and optimization.

where η_0 is the free-space impedance. Formally, Eq. (12) should be evaluated for the secondary patterns. However, these patterns are highly directive and have many side lobes, particularly for electrically large reflectors. An accurate numerical integration would be time demanding and require large data storage. Note that, on the other hand, the primary patterns have a relatively low gain and have a smooth angular variation. These patterns can be used in (12), provided that $T_{\text{ext}}(\Omega)$ represents the external temperature distribution as seen by the array feed. This approach neglects the spillover

contribution due to scattering at the focus-box and the struts. This procedure is similar to a conventional (spillover) noise temperature calculation of a feed.

The signal-wave vector $\mathbf{e}_{\text{ant}}^p$ at the outputs of the antenna array (see Fig. 2, block 3) is calculated as

$$\mathbf{e}_{\text{ant}}^p = \mathbf{L}\mathbf{V}_{\text{oc}}^p \quad \text{where} \quad p \in \{\text{CO}, \text{XP}\} \tag{13}$$

where the elements of vector $\mathbf{V}_{\text{oc}}^p$ are the voltages induced at the open-circuited antenna ports due to an externally applied incident plane-wave field $\boldsymbol{E}_{\text{i}}^p$. More specifically, the nth element of this vector is defined as

$$v_{\text{oc},n}^p = \frac{4\pi e^{jk_0}}{j\omega\mu_0}\left(\boldsymbol{E}_{\text{i}}^p \cdot \boldsymbol{F}_n\right) \tag{14}$$

where $\{\boldsymbol{F}_n\}$ are the N secondary far-field patterns (after reflection from the dish). These patterns are computed by the GRASP PO/PTD solver from the primary patterns that have been computed by CAESAR's MoM solver.

Next, the overall (reflector-array-receiver) system noise-wave correlation matrix $\mathbf{C}$ and the signal-wave vectors $\mathbf{e}^{\text{CO}}$ and $\mathbf{e}^{\text{XP}}$ are computed (see Fig. 2, block 3) using connection matrix theory [22]. The TSA array has been treated in this paper as a metal-only structure and the antennas have been excited by voltage-gap generators that are placed across the slot-line sections, while the wideband MicroStrip Feeds (MSFs) have been separately modeled by non-radiative microwave-circuit devices [23]. Hence, they appear as separate receiver components in the diagram. This approach allows one to significantly reduce the computational burden and has demonstrated a good agreement between measurements and simulations [18]. In particular, the differences between the measured and simulated coupling coefficients of a large array were found to be less than $\sim 20\%$ over the entire frequency range, which is good in view of the antenna complexity and manufacturing tolerances of the TSAs.

Since the matrix $\mathbf{C}$ and the signal vectors $\mathbf{e}^{\text{CO}}$ and $\mathbf{e}^{\text{XP}}$ have been determined, the optimum beamformer weights can be calculated for the specified observation directions and selected performance criteria. These criteria (see Sec. II-A) include: (i) the directive gain optimization of the secondary beam pattern in the direction of the far-field source [see Eq. (3)]; (ii) the maximum beam sensitivity in the observation direction corresponding to the center of the main beam of the secondary-field pattern [see Eq. (2)], and; (iii) the maximum beam sensitivity but with constraints at the cross-over points between adjacent main beams [see Eq. (4)].

The final step is to post-process the computed data and to visualize the quantities of interest as listed in the last step of Fig. 2.

IV. DESCRIPTION OF THE PROTOTYPE SYSTEM

The simulation and measurement results in this paper are based on the second APERTIF prototype. This PAF occupies nearly the entire available area (1 m^2) in the focus box of the WSRT antenna (Fig. 3 at the top right corner). The array consists of 2×72 aluminium TSA elements with a pitch of 11 cm (0.52λ at 1420 MHz) on a rectangular 8×9 grid. Each TSA is fed by a wideband microstrip feed which has
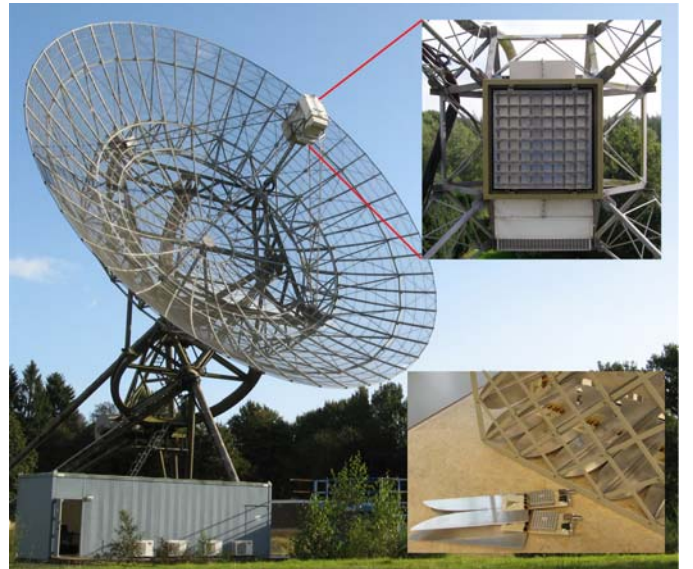

Fig. 3. A 25-m reflector antenna of the Westerbork Synthesis Radio Telescope (left), the PAF installed at the focus (top right), and a PAF element with LNA assembly (bottom right).
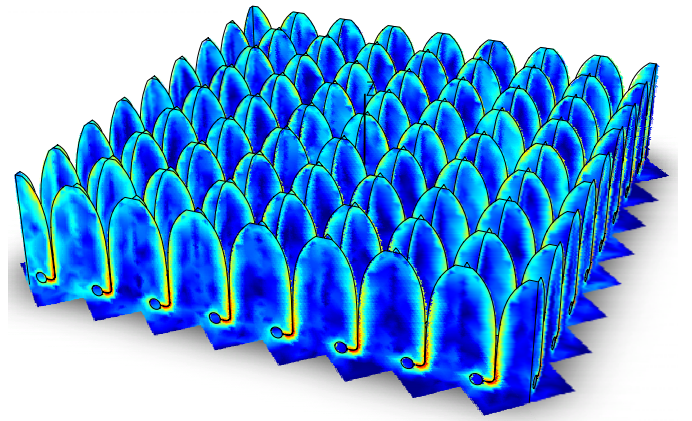

Fig. 4. EM-model of the PAF comprised of $8 \times 9 \times 2$ Tapered Slot Antenna (TSA) elements. The current distribution is displayed for the case that all elements are equally excited.

been integrated with an LNA on a printed circuit board, as illustrated in Fig. 3 (bottom-right). This design features a very short transmission line between the antenna and the LNA, since the circular slotline cavity has been moved sideways as illustrated in Fig. 4. The elements are connected through extruded profiles which improve the mechanical and electrical stability and allow for easy replacement of single elements. More details on the array design can be found in [24].

The RF signals received by the PAF are transported to a shielded cabin (Fig. 3 bottom left) using coaxial RF cables. Because only 56 receivers are available, a selection of the elements is made. The antenna output signals are down-converted, digitized and stored on disk so that the beamforming can be performed off-line. The unused elements are terminated with LNAs with loads at their outputs. The LNAs operate at ambient temperature and have a minimum equivalent noise-temperature

that varies between 35 and 45 K over the frequency range from 1.0 to 1.75 GHz (for a 50-Ohm source impedance).

V. NUMERICAL AND EXPERIMENTAL RESULTS

A. Simulation details

Fig. 4 shows the 144-element dielectric-free array model. Its impedance and radiation patterns have been simulated by CAESAR. The simulated primary-field patterns of the embedded array elements were exported to the CAESAR-GRASP toolbox and used to perform the overall system analysis and optimization of beamformer weights (see Sec. III). The model parameters of the microstrip feed, as defined in [23], are $N = 5$, $L_1 = 34.6$ mm, $L_2 = 2$ mm, $n = 0.97$. The transmission line length L_1 includes the equivalent connector length, and is much smaller than that of a conventional microstrip line feeding a TSA (see Table I in [18], as an example). The L_2 is the length of the transmission line between the TSA slot and the beginning of the triangular stub. The parameter n has been obtained by a least-squares fit of the port impedance of the cascaded model (antenna+feed) onto the (measured) reference impedance. The details of this procedure can be found in [23], [18].

The system noise temperature is calculated as a sum of several contributions due to external and internal noise sources. The former is the ground noise picked up due to spillover, which is computed using the simulated illumination pattern of the reflector (i.e. the primary pattern of the feed). The internal noise contribution includes two components:

- the thermal antenna noise due to the losses in the conductor material of TSAs and microstrip feeds. The conductor losses are computed through the evaluation of the antenna's radiation efficiency using the methodology detailed in [25].
- multi-channel receiver noise which is calculated using an equivalent single-channel receiver representation of the system [26]. This noise component accounts for the antenna-LNA impedance noise mismatch effect and minimal noise of LNAs. In this representation, the system noise temperature contribution is referenced to the sky.
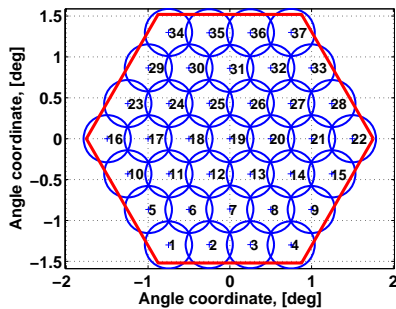
Fig. 5.   Enumeration and arrangement of the main beams on the sky.

B. Simulated Primary Patterns and Aperture Efficiency

Within the APERTIF field of view, 37 beams on a hexagonal grid are formed to create the required continuous 8 square

degrees field of view. Fig. 5 shows the arrangement and enumeration of the beams on the sky. A sensitivity simulation has been carried out for three beamforming scenarios:

(a) primary pattern cuts for $\phi = 0^o$

(b) primary pattern cuts for $\phi = 45^o$

(c) primary pattern cuts for $\phi = 90^o$
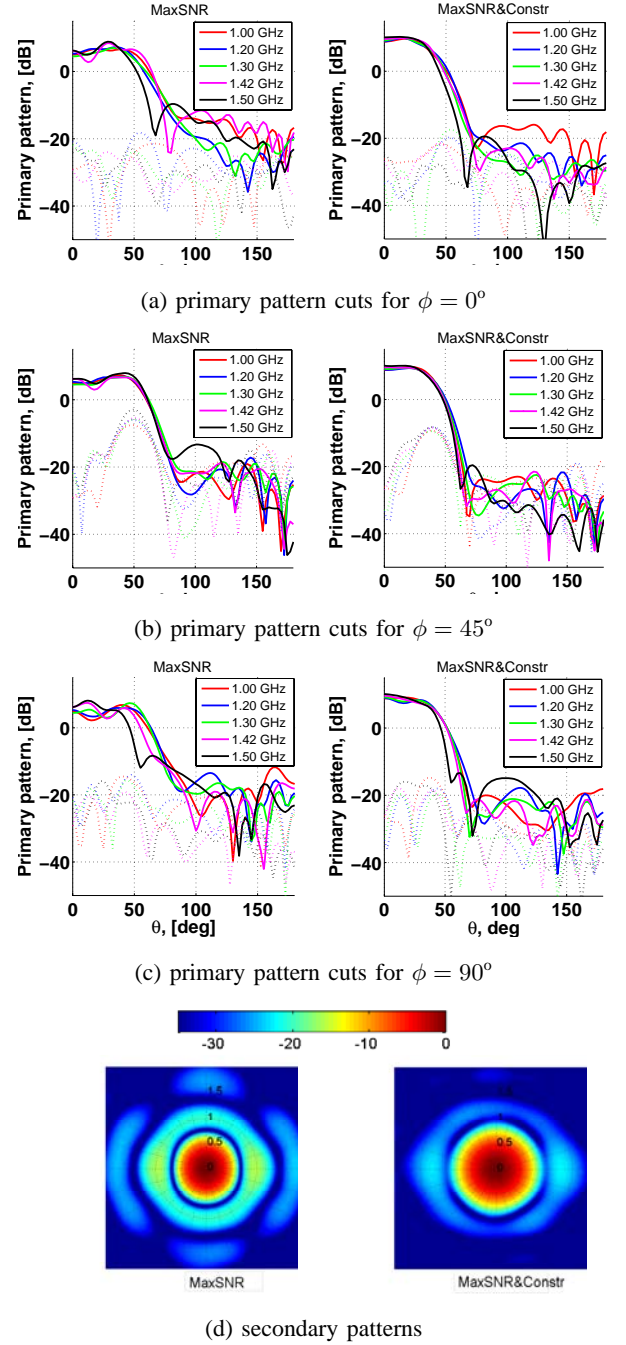
(d) secondary patterns

Fig. 6.   (a)–(c) Simulated PAF primary pattern cuts, and (d); secondary patterns for an on-axis beam using weights obtained without constraints (left-hand column) and with constraints (right-hand column). The co- and cross-polarization components of the primary patterns are plotted in solid and dotted lines respectively. The secondary patterns are shows for 1.42 GHz.

TABLE I
THE VALUES OF CONSTRAINTS VS. FREQUENCY IN GHZ.

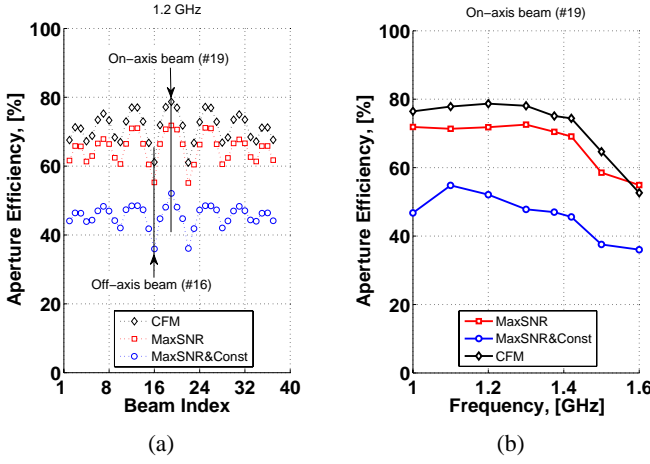| Freq.	1.00	1.10	1.20	1.30	1.375	1.42	1.50	1.60
Values	0.91	0.88	0.86	0.85	0.84	0.83	0.84	0.83

Fig. 7. Simulated aperture efficiency for the on-axis beam at 1.2 GHz versus frequency (b), and for 37 beams within the FOV (a).
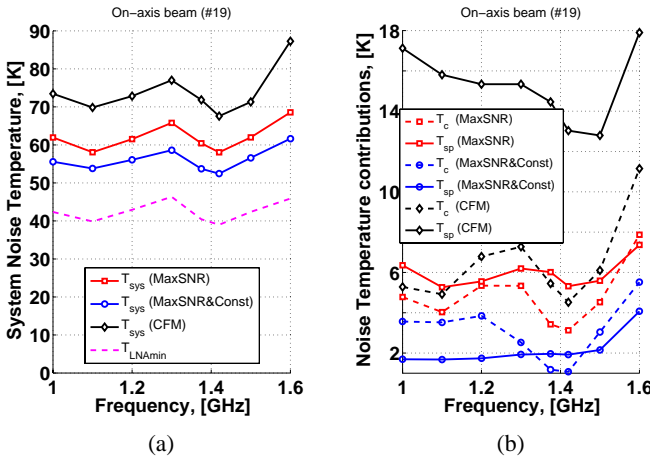

Fig. 8. (a) Simulated system noise temperature T_{sys} for the on-axis beam and the minimal noise temperature of the LNA T_{min}. (b) Noise contributions due to spillover (T_{sp}) and noise coupling effects in the receiver (T_c).

(i) Conjugate Field Matching (CFM); (ii) Maximum Sensitivity (MaxSNR) in the direction of the beam center, and (iii) MaxSNR with directional constraints. Starting from (ii), a more uniform sensitivity over the FOV can be obtained by broadening each beam and making it more rotational symmetric (homogeneous). This is realized by imposing additional constraints on the cross-over points between adjacent beams. There are six such points for each beam for the grid shown in Fig. 5. In this study the cross-over points are located $0.25°$ from the beam center. In an iterative process, the beam center sensitivity is maximized with identical constraints applied at the cross-over points such that the sensitivity loss at the beam center is at most 10% with respect to the sensitivity without constraints. The calculation is repeated for every frequency point. The values of the resulting constraints over the frequency band are listed in Table I.

Fig. 6 shows the simulated primary pattern cuts and the corresponding secondary patterns for the broadside beam (index #19), as an example. As one can see, the primary patterns realizing the maximum SNR (column on the left) are wide and with sharp cut-off toward the rims of the dish ($\theta_{sub} = 71°$). The

primary patterns for the constraint optimization (column on the right) are narrower and more rotationally symmetric which results in the broadening and the more homogeneous secondary beam on the sky [see Fig. 6(d)]. The beam symmetry is almost the same for off-axis directions of observation (due to identical constraints). This beam shaping can significantly reduce the complexity of the beam calibration models needed to reconstruct the original image [27]. On the contrary, the beams realizing the maximum sensitivity in their centers have very different shapes for all directions. The penalty of this constraint optimization is a reduced aperture efficiency with respect to the maximum SNR beamformer, as demonstrated in Fig. 7(a) for 37 beams at 1.2 GHz and in Fig. 7(b) over the frequency bandwidth for the on-axis beam. Furthermore, Fig. 7(b) also shows that at frequencies higher than 1.42 GHz, at which the element spacing is larger than 0.5λ, the efficiency rapidly degrades for all beamforming scenarios as a result of focal field under-sampling [28].

C. Simulated System Noise Temperature

Fig. 8 shows the system noise temperature T_{sys} and its dominant contributions for the three beamforming scenarios. Here, T_{sp} denotes the spillover noise component and T_c is the noise coupling contribution due to the impedance noise mismatch, which is a combined effect of the active reflection coefficients of the array elements and the LNA noise parameters [29], [30]. As expected, the CFM beamformer leads to the highest system temperature, as it maximizes the received power in the absence of the noise sources. Therefore, the ground noise pick-up is very high (13-18 K). In contrast, T_{sp} for the MaxSNR beamformer is significantly smaller (5–8 K), and virtually zero for the constrained (LCMV) beamformer. The T_c exhibits similar dependence on the beamforming schemes, and takes the lowest values for the constrained optimization (and the highest values for CFM). The reason for these low values is that for the constrained beamformer, a relatively small number of array elements are strongly weighted such that the resulting active element reflection coefficients lead to the lower noise coupling effects. Table. II shows the relation between the number of highly weighted array elements, the maximum value of the element active reflection coefficients (over the entire FOV and bandwidth), and the corresponding noise matching efficiency. This efficiency is a figure of merit for the quality of the realized active impedance match with LNAs [30]. More simulation details on the behavior of the active reflection coefficients as well as the radiation efficiency for different beamforming scenarios can be found in [24]. The system noise temperatures of off-axis beams are not shown, since these assume at most 10% higher values than that of the on-axis beam due to the dominant contribution of T_{min} of the LNAs [see Fig. 8(a)].

D. Simulated Sensitivity

Fig. 9 shows the simulated sensitivity over the FOV, normalized to its peak level. The black line indicates the 8 square degrees FOV. The sensitivity over the FOV was determined by calculating the square root of the sum of the squared

TABLE II
THE EFFECT OF THE BEAMFORMING SCENARIO ON THE ARRAY ELEMENT
ACTIVE IMPEDANCE MATCH WITH LNAS.(THE NUMBER OF HIGHLY
WEIGHTED ELEMENTS IS GIVEN FOR 1.2 GHz).

The beamforming scenario	CFM	MaxSNR	MaxSNR & constr
# elements with weights $|w_n| > -12$ dB	24	18	12
$|\Gamma_{act}|_{max}$ over FOV and BW, [dB]	-10	-13.5	-15
The noise matching efficiency η_n	0.84	0.88	0.91

beam sensitivities. This summation assumes that the system noise of adjacent beams is uncorrelated. This condition is obviously true for conventional systems where the beams are measured consecutively in time. With PAFs, the beams are measured simultaneously and theoretically a correlation can exist. However, Willis [31] showed that noise correlation is not of a major concern for interferometric imaging because the phase rotations inherent in interferometric imaging decorrelate the noise. Fig. 9 compares the telescope's sensitivities (for a single pointing direction of the dish with 37 simultaneously formed beams) that were computed for the maximum SNR beamformer with (b) and without (a) constraints on the beam shapes. These results clearly demonstrate the advantage of the constrained optimization to reduce the sensitivity variation over the wide FOV and frequency bandwidth (compare the sensitivities at 1.2 GHz, 1.42 GHz and 1.6 GHz). These images have been normalized to their maxima in order to illustrate their different shapes. The absolute sensitivities at the beam centers using the MaxSNR beamformer are 10% higher. The average absolute values of the sensitivities for the considered beamformers and the corresponding maximum sensitivity ripple (defined as the average relative difference between its maximum and minimum sensitivity value) are shown in Fig. 10(a) and (b). It is observed that the MaxSNR beamformer maximizes the sensitivity at the beam centers, but results in a large sensitivity ripple over the FOV. When the number of beams is increased up to 61, the realized sensitivity ripple is almost as small as that for the 37 closely overlapping beams subject to the constrained optimization [see Fig. 10(c)].

E. Measured Sensitivity

The measurements of the APERTIF prototype at the WSRT are used for the experimental determination of the optimal beamformer weights (as described in Sec. II) and the corresponding sensitivity. Cassiopeia A has been used as the astronomical source. Thus far, the sensitivities have been computed using all 72 horizontally-polarized elements per beam. Fig. 11 shows a comparison between simulated sensitivities when using 52, 72 and 144 elements. The measured sensitivities are for 52 elements. The beams were optimized for MaxSNR without constraints. First of all, the correspondence between the simulated and measured sensitivities is very good. The relative sensitivity difference at the centers and cross-over points is less than 6% and 15%, respectively. The sensitivity of the 144 element system is only a few percent higher than when 72 elements are used.

Fig. 12 compares the simulated and measured sensitivity over the entire FOV. A maximum sensitivity beam is formed
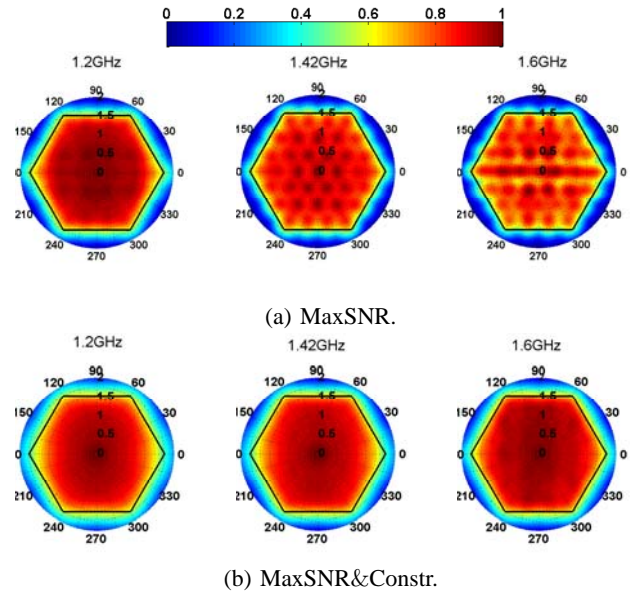

(a) MaxSNR.

(b) MaxSNR&Constr.

Fig. 9. Simulated sensitivity over the FOV (normalized to its peak value) at three frequencies by combining 37 beams. The beamformer weights were applied to 72 equally-oriented array elements to generate each of the 37 beams with (a) the maximum sensitivity (MaxSNR) at its center and (b) with directional constraints (MaxSNR&Constr). The black line indicates the required FOV.

for each pixel in these plots, i.e. for 31×31 beam centers in total. The relative difference between the simulations and the measurements is 11% near the center of the FOV. Similar agreement was achieved for the first prototype model, for which experimentally determined weights were used [6]. This relative difference increases up to 25–30% at the edges of the FOV. We attribute this discrepancy to a modeling error of the edge elements due to the absence of the surrounding support structure in the simulation (such as the feed box and struts) [32]. The edge elements receive high weights when forming beams near the edges of the FOV and, hence, become more important. More results on the experimental verification of the developed numerical approach and simulation tool can be found in [33].

VI. POLARIZATION DISCRIMINATION

In this section, the polarimetric behavior of the PAF is characterized by evaluating two figures of merit: the beam orthogonality ρ_{cor}, which describes the orthogonality of the beams formed by the PAF system (as introduced in Sec. II-C), and the Intrinsic Cross-Polarization Ratio (IXR) [see Eq. (10)]. The IXR also accounts for gain differences between the beam pairs, whereas ρ_{cor} does not. Fig. 13 presents the simulated beam orthogonality at 1.2 GHz for two realizations of the MaxSNR beamformers. For the image on the left two beams are formed, each using only 72 identically polarized elements per beam. The image on the right is obtained when all 144 elements are used to form each beam. Because of the larger degrees of freedom to control the beam polarimetrically, the 144-element beamformer results in the highest polarization discrimination. For the sake of comparison, Fig. 14 illustrates the simulated IXR for the same situations.
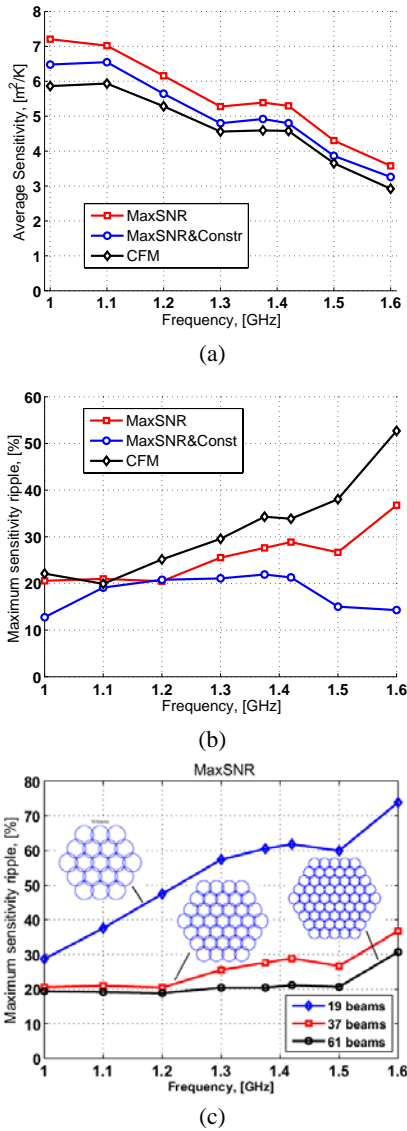
(a)

(b)

(c)

Fig. 10. (a) Simulated average sensitivity over the FOV using 37 beams. (b) Maximum sensitivity ripple for the three beamforming scenarios for 37 beams, and (c) the maximum SNR scenario for 19, 37 and 61 beams.
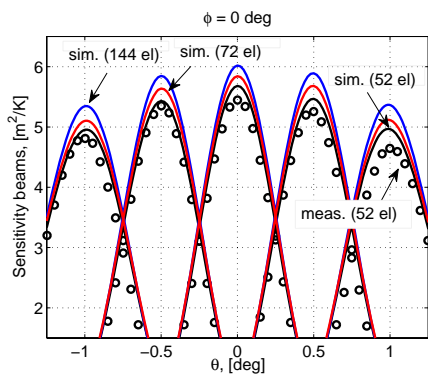

Fig. 11. Simulated and measured sensitivities of 5 beams (beam indices #17 − #21) using the MaxSNR beamformer at 1.42 GHz. The simulated beams are shown for 3 beamformer realizations, using 52, 72 and 144 elements. The measured sensitivity was determined using only 52 elements.
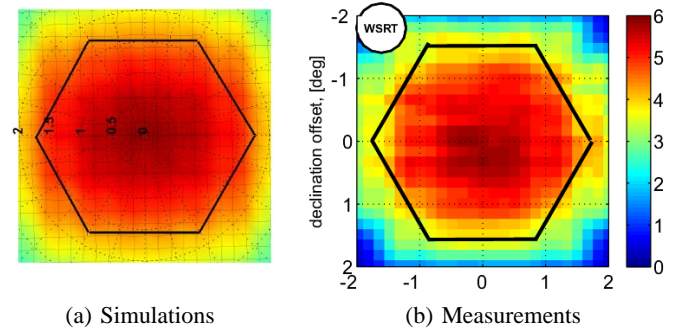

(a) Simulations   (b) Measurements

Fig. 12. (a) Modeled, and (b) measured sensitivities over the FOV. The black line indicates the required FOV. The white circle in (b) indicates the smaller FOV of the existing WSRT system.

One observes from Figs. 13 and 14 that the ρ_{cor}^{-1} and IXR values are comparable, the main difference being that the IXR is more uniform over the FOV, likely because the beam gain difference is also taken into account.

In Fig. 15, the simulated IXR and the inverse of the beam orthogonality - averaged over the FOV - are shown as function of frequency, for the bi-scalar and full-polarization beamformers. It is observed that the accuracy to perform an adequate polarization discrimination increases in case all 144 element are actively beamformed, relative to the situation when only 72 equally-oriented elements are used to form a polarimetric beam pair. In either case, the figure of merits are better than 22 dB for 80% of the imaged area on the sky. A comparative analysis of the average IXR (and ρ_{cor}^{-1}) for the MaxSNR beamformers with and without constraints demonstrates a very similar behavior over the frequency band.
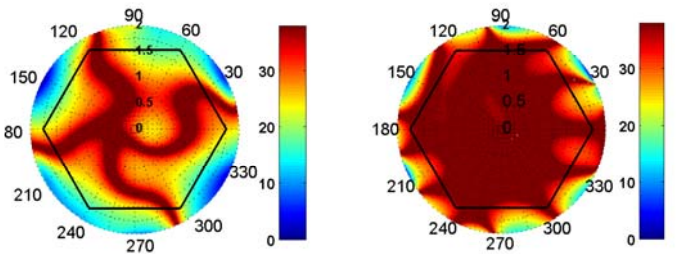

Fig. 13. The inverse of the simulated beam orthogonality (ρ_{cor}^{-1}) over the FOV when 72 (on the left) and 144 (on the right) elements are used in the MaxSNR beamformer. Frequency is 1.2 GHz and the scale is logarithmic.

VII. CONCLUSIONS

A numerical approach has been developed to model a Phased Array Feed (PAF) system comprised of an electrically large reflector, an array feed of many mutually-coupled antenna elements, low-noise amplifiers, and a beamformer. This approach has been experimentally verified for the APERTIF system – a PAF prototype for the Westerbork Synthesis Radio Telescope. The agreement between the simulated and measured beam sensitivities is very good, *viz.*; the relative difference between the measurements and simulations for
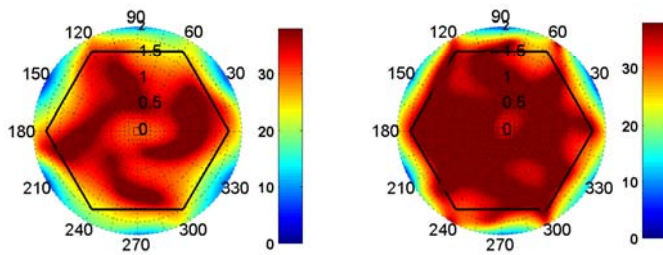
Fig. 14.   Simulated IXR over the FOV when 72 (on the left) and 144 (on the right) elements are used in the MaxSNR beamformer. Frequency is 1.2 GHz.
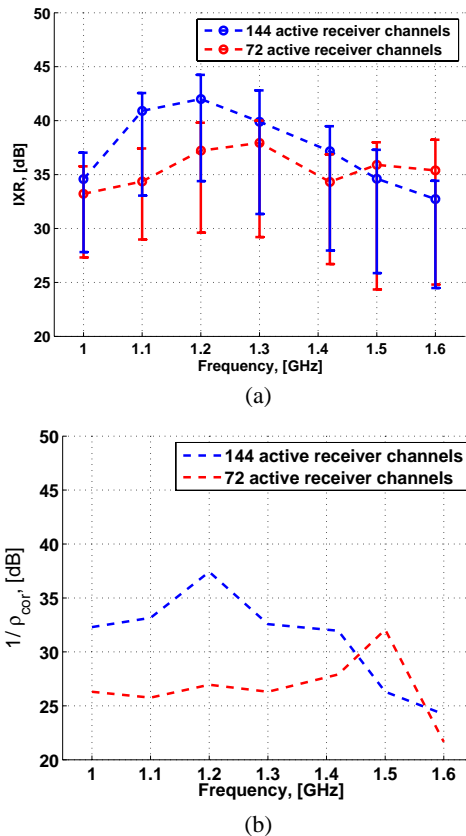

Fig. 15.   (a) Simulated IXR, and (b) inverse of the beam orthogonality versus frequency for the MaxSNR beamformers using 72 and 144 elements. The solid lines show the average values over the FOV. The vertical bars indicate the range of the IXR over the FOV.

31×31 beam directions is smaller than 11% and about 30% for beams near the center and edges of the field of view (FOV), respectively. This is a satisfactory result, since the system is very complex while the model does not account for reflector-feed interactions and the actual feed box environment. To the authors' best knowledge, it is the best agreement thus far presented for such a complex system within the PAF community.

A linear constrained minimum variance (LCMV) beamformer has been employed to optimize the beam shapes of the APERTIF prototype system. The conventional maximum SNR beamformer maximizes the sensitivity at one beam-center direction, while the constraint SNR beamformer also improves the rotational symmetry of the beam. The transition between adjacent beams becomes smoother and the sensitivity is more uniform over a wide FOV and frequency bandwidth. This reduces the complexity of the beam calibration model and eases the reconstruction of the original image. The sensitivity ripple of the modeled PAF system with 37 overlapping beams has been reduced from $20-35\%$ to $12-22\%$ over the 1.0-1.75 GHz frequency band, while compromising the peak sensitivity no more than 10% with respect to the MaxSNR scheme. The MaxSNR scheme yields high sensitivity, but requires almost twice as many beams to cover the same area of the sky with a sensitivity ripple less than 20% over the frequency band.

The polarization discrimination capability of the PAF has been analyzed by considering a pair of beamformer output voltage vectors which are the system responses to two orthogonally-polarized incident fields of unit intensity from the same direction. Two figures of merit have been considered: 1) the cross correlation between the beamformer output voltage vectors, and 2) the Intrinsic Cross-Polarization Ratio (IXR). The numerical results show that both figures of merit are larger than 22 dB over 80% of the FOV. The IXR seems most suited to measure the polarimetric beam independency, since it not only measures the orthogonality of a beam pair, but also quantifies its gain differences.

It has been shown that the beam sensitivity can be increased with $3-4\%$ when all the array elements are used to form a polarimetric beam pair (a 'full-polarization' beamformer), as opposed to forming a beam pair of which each beam is realized by using the corresponding equally oriented array elements (a 'bi-scalar' beamformer). However, this is a minor improvement knowing that the complexity of the beamformer must be doubled. This in turn shows that the instrument has good intrinsic polarization properties.
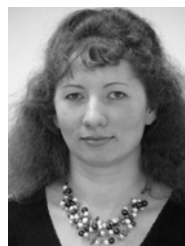
VIII. Acknowledgement

References

[1] C. Carilli and S. Rawlings, Eds., *Science with the Square Kilometre Array*.   Amsterdam: Elsevier, Dec. 2004.

[2] SKA Science Working Group. (2009, Oct.) Design reference mission for the ska-mid and ska-lo. 091001_DRM_v0.4.pdf. [Online]. Available: http://www.skatelescope.org/pdf/

[3] D. DeBoer, R. Gough, J. Bunton, T. Cornwell, R. Beresford, S. Johnston, I. Feain, A. Schinckel, C. Jackson, M. Kesteven, A. Chippendale, G. Hampson, J. O'Sullivan, S. Hay, C. Jacka, T. Sweetnam, M. Storey, L. Ball, and B. Boyle, "Australian ska pathfinder: A high-dynamic range wide-field of view survey telescope," *IEEE Trans. Antennas Propagat.*, vol. 97, no. 8, pp. 1507–1521, Aug. 2009.

[4] J. D. Bunton. (2003, Sept.) Figure of merit for ska survey speed. Bunton_Survey_speed.pdf. [Online]. Available: http://www.skatelescope.org/documents/

[5] A. Thompson, J. Moran, and G. Swenson, *Interferometry and Synthesis in Radio Astronomy*. New York: John Wiley and Sons, Inc., 2001.

[6] M. V. Ivashina, O. A. Iupikov, R. Maaskant, W. A. van Cappellen, L. Bakker, and T. Oosterloo, "Off-axis beam performance of focal plane arrays for the westerbork synthesis radio telescope initial results of a prototype system," in *Proc. IEEE AP-S International Symposium*, Charleston, USA, June 2009, pp. 1522–3965.

[7] W. A. van Cappellen, L. Bakker, and T. A. Oosterloo, "Experimental results of a 112 element phased array feed for the westerbork synthesis radio telescope," in *Proc. IEEE AP-S International Symposium*, Charleston, USA, June 2009, pp. 1522–3965.

[8] R. Maaskant, "Analysis of large antenna systems," Ph.D. dissertation, Eindhoven Univ. of Technology, Eindhoven, 2010. [Online]. Available: http://alexandria.tue.nl/extra2/201010409.pdf

[9] D. K. Cheng and F. I. Tseng, "Maximisation of directive gain for circular and elliptical arrays," *Proc. Inst. Elec. Eng.*, pp. 589–594, May 1967.

[10] Y. T. Lo and S. W. Lee, "Optimization of directivity and signal-to-noise ratio of an arbitrary antenna array," *IEEE Trans. Antennas Propagat.*, vol. 54, no. 8, pp. 1033–1045, Aug. 1966.

[11] H. L. van Trees, *Optimum Array Processing*. New York: John Wiley and Sons, Inc., 2002.

[12] B. D. Jeffs and K. F. Warnick, "Signal processing for phased array feeds in radio astronomical telescopes," *IEEE Trans. Signal Processing*, vol. 2, no. 5, pp. 635–646, Oct. 2008.

[13] S. W. Wedge and D. B. Rutledge, "Wave techniques for noise modeling and measurement," *IEEE Trans. Antennas Propagat.*, vol. 40, no. 11, pp. 2004–2012, Nov. 1992.

[14] M. V. Ivashina, M. Kehn, P.-S. Kildal, and R. Maaskant, "Decoupling efficiency of a wideband vivaldi focal plane array feeding a reflector antenna," *IEEE Trans. Antennas Propagat.*, vol. 57, no. 2, pp. 373–382, Feb. 2009.

[15] P. J. Wood, *Reflector antenna analysis and design*. Stevenage, U.K., and New York: IEE, Peter Peregrinus LTD., 1980.

[16] K. F. Warnick, B. D. Jeffs, J. R. Fisher, and R. Norrod, "Beamforming and imaging with the byu/nrao l-band 19-element phased array feed," in *13th Int. Symp. on Antenna Tech. and Applied Electromagnetics (ANTEM)*, Banff, AB, Canada, Feb. 2009, pp. 1–4.

[17] A. Ludwig, "The definition of cross polarization," *IEEE Trans. Antennas Propagat.*, vol. 21, no. 1, pp. 116–119, Jan. 1973.

[18] R. Maaskant, M. V. Ivashina, O. Iupikov, E. A. Redkina, S. Kasturi, and D. H. Schaubert, "Analysis of large microstrip-fed tapered slot antenna arrays by combining electrodynamic and quasi-static field models," *IEEE Trans. Antennas Propagat.*, accepted for publication.

[19] J. P. Hamaker, J. D. Bregman, and R. J. Sault, "Understanding radio polarimetry. mathematical foundations," *Astron. Astrophys. Suppl. Ser.*, vol. 117, pp. 137–147, 1996.

[20] T. D. Carozzi and G. Woan. (2009, Aug.) A fundamental figure of merit for radio polarimeters. [Online]. Available: http://arxiv.org/abs/0908.2330v1

[21] R. Maaskant and B. Yang, "A combined electromagnetic and microwave antenna system simulator for radio astronomy," in *Proc. European Conference on Antennas and Propag. (EuCAP)*, Nice, France, Nov. 2006, pp. 1–4.

[22] J. A. Dobrowolski, *Introduction to Computer Methods for Microwave Circuit Analysis and Design*. Warsaw University of Technology: Artech House, 1991.

[23] M. V. Ivashina, E. A. Redkina, and R. Maaskant, "An accurate model of a wide-band microstrip feed for slot antenna arrays," in *Proc. IEEE AP-S International Symposium*, Hawaii, USA, June 2007, pp. 1953–1956.

[24] M. Arts, M. Ivashina, O. Iupikov, L. Bakker, and R. van den Brink, "Design of a low-loss low-noise tapered slot phased array feed for reflector antennas," in *Proc. European Conference on Antennas and Propag. (EuCAP)*, Barcelona, Spain, Apr. 2010.

[25] R. Maaskant, D. J. Bekers, M. J. Arts, W. A. van Cappellen, and M. V. Ivashina, "Evaluation of the radiation efficiency and the noise temperature of low-loss antennas," *IEEE Antennas Wireless Propagat. Lett.*, vol. 8, no. 1, pp. 1166–1170, Dec. 2009.

[26] M. V. Ivashina, R. Maaskant, and B. Woestenburg, "Equivalent system representation to model the beam sensitivity of receiving antenna arrays," *IEEE Antennas Wireless Propagat. Lett.*, vol. 7, no. 1, pp. 733–737, 2008.

[27] O. Iupikov and M. Ivashina, "Reducing a complexity of the beam calibration models of phased-array radio telescopes," in *submitted to European Conference on Antennas and Propag. (EuCAP)*, Rome, Italy, Apr. 2011.

[28] M. V. Ivashina, M. Ng Mou Kehn, and P.-S. Kildal, "Optimal number of elements and element spacing of wide-band focal plane arrays for a new generation radio telescope," in *Proc. European Conference on Antennas and Propag. (EuCAP)*, Edinburg, UK, Nov. 2007, pp. 1–4.

[29] R. Maaskant and B. Woestenburg, "Applying the active antenna impedance to achieve noise match in receiving array antennas," in *Proc. IEEE AP-S International Symposium*, Honulollu, Hawaii, June 2007, pp. 5889–5892.

[30] K. F. Warnick, E. E. M. Woestenburg, L. Belostotski, and P. Russer, "Minimizing the noise penalty due to mutual coupling for a receiving array," *IEEE Trans. Antennas Propagat.*, vol. 57, no. 6, pp. 1634–1644, June 2009.

[31] A. G. Willis, B. Veidt, and A. Gray, "Focal plane array simulations with meqtrees 1: Beamforming," National Research Council of Canada, Dominion Radio Astrophysical Observatory, Penticton, BC, Canada V2A 6J9, Tech. Rep. Feb., 2009.

[32] N.-T. Huang, R. Mittra, M. V. Ivashina, and R. Maaskant, "Numerical study of a dual-polarized focal plane array (fpa) with vivaldi elements in the vicinity of a large feed box using the parallelized fdtd code gems." in *Proc. IEEE AP-S International Symposium*, Charleston, USA, June 2009, pp. 1522–3965.

[33] M. Ivashina, O. Iupikov, and W. van Cappellen, "Extending the capabilities of the grasp and caesar software to analyze and optimize active beamforming array feeds for reflector systems," in *Proc. Int. Conf. on Electromagn. in Adv. Applicat. (ICEAA)*, Syndey, Sept. 2010, pp. 197–200.

Marianna V. Ivashina was born in Ukraine in 1975. She received the combined B.Sc/M.Sc. degree and Ph.D. both in Electrical Engineering from the Sevastopol National Technical University (SNTU), Sevastopol, Ukraine, in 1995 and 2000, respectively. From 2001 to 2004 she was a Postdoctoral Researcher and from 2004 till 2010 an Antenna System Scientist at ASTRON. During this period she has carried out research on an innovative focal plane array (phased array feed) technology for a new generation radio telescope, known as the Square Kilometre Array (SKA). In 2002, she also stayed as a visiting scientist at the European Space Agency (ESA), ESTEC in the Netherlands, where she studied multiple-beam array feeds for the satellite telecommunication system Large Deployable Antenna (LDA). She received the URSI Young Scientists Award for GA URSI, Toronto, Canada (1999), APS/IEEE Travel Grant, Davos, Switzerland (2000), the 2nd Best Paper Award ('Best team contribution') at the ESA Antenna Workshop (2008) and the VINNOVA - Marie Curie Actions International Qualification Fellowship (2009) for a joint project with Chalmers University of Technology (Sweden), at which she will be employed for 2 years from January 2011. Her research interests are focal plane arrays, array feeds for reflector antennas, wide-band receiving arrays, and radio astronomy.

Oleg Iupikov received his M.Sc. degree (*cum laude*) in Electrical Engineering from the Sevastopol National Technical University, Ukraine, in 2006. After graduating he has been working for a year at the Radio Engineering Bureau in Sevastopol. Since 2007, he is working toward his Ph.D. degree in the field of phased array feeds and their optimization. He received a Marie Curie visitor grant to perform scientific research at the Netherlands Institute for Radio Astronomy (ASTRON) during the period of 2008-2010.

Rob Maaskant received the M.Sc. and Ph.D. degree, both *cum laude*, in Electrical Engineering from the Eindhoven University of Technology, the Netherlands, in 2003 and 2010, respectively. Since 2003, he has been an antenna research engineer at the Netherlands Foundation for Research in Astronomy (ASTRON) where his research is carried out in the framework of the Square Kilometre Array (SKA) radio telescope project. He received the 2nd Best Paper Award ('Best team contribution') at the ESA Antenna Workshop (2008). In 2010, the Netherlands Organization for Scientific Research (NWO) awarded him the Rubicon grant. This grant allows him to perform two years of postdoctoral research at the Chalmers University of Technology, Sweden. Currently, his research interests include the development of numerically efficient integral-equation techniques for large finite array antennas, the characterization and design of antenna array receiving systems.

Wim van Cappellen Wim van Cappellen obtained his MSc degree (*cum laude*) in Electrical Engineering from Delft University of Technology, The Netherlands, in 1998. From 1998 to 2001 he was with Thales Nederland B.V. to study innovative concepts for naval radar systems. Since 2001, he is with the Netherlands Institute for Radio Astronomy (ASTRON) where he is now responsible for the coordination and technical program of the Antenna Group. His research interests are ultra wideband antenna arrays and phased array feeds for application in radio-astronomical low-noise receiving systems. He is currently leading the phased array feed project APERTIF.

Tom Oosterloo Tom Oosterloo is Senior Astronomer at the Netherlands Institute for Radio Astronomy (ASTRON) and Assistant Professor at the Kapteyn Astronomical Institute of Groningen University. After finishing his PhD in 1988, he held several postdoc positions in both radio and optical astronomy. Since 1999 he works at ASTRON where he spends most of his time on astronomical research but he is also involved in technical programs the relating to the telescopes operated by ASTRON. He is Principal Investigator of APERTIF, the Phased Array Feed upgrade of the Westerbork Synthesis Radio Telescope. He is member of the time allocations committee of several radio telescopes. He is (co)author of 115 peer-reviewed papers.